JOURNAL OF MATERIALS SCIENCE 23 (1988) 2348–2354

Stability of Si_3N_4–Al_2O_3–ZrO_2 composites in oxygen environments

A. BELLOSI, P. VINCENZINI, G. N. BABINI
Research Institute for Ceramics Technology, National Research Council, Faenza, Italy

Oxidation of dense Si_3N_4–Al_2O_3–ZrO_2 and Si_3N_4–Al_2O_3 compacts, at 873–1773 K and 98 KPa air atmosphere, results in two different parabolic oxidation regimes. Oxygen diffusion is likely to be the governing step at low temperature ($T < \sim 1623$ K ($\Delta H = \sim 100$ kJ mol^{-1})), whereas at $T > \sim 1623$ K ($\Delta H = \sim 800$ kJ mol^{-1}) metal cation diffusion through the grain boundary phase appears limiting. The excellent stability in oxygen environments of the Si_3N_4–Al_2O_3–ZrO_2 composites compared to other ZrO_2–Si_3N_4 materials derives from (i) absence of easy-to-oxidize Zr–O–N phases; (ii) reduced amount of grain boundary phase, and possibly (iii) decreased solubilization rate of the nitride phases in the high viscous oxide film.

1. Introduction

Most of the studies on oxidation of hot pressed silicon nitride (HPSN) stress the decisive role of transport phenomena. Diffusion of additives and impurities within the grain boundary phase has been generally suggested [1–5] to be the rate governing step for the parabolic oxidation behaviour observed in a range of test conditions.

Oxidation kinetics for dense Si_3N_4-based ceramics have been discussed in detail in terms of the amount of additive [5–11], the presence of easy-to-oxidize phases which readily form in Si_3N_4–Y_2O_3 [6, 8], Si_3N_4–MgO–ZrO_2 and Si_3N_4–MgO–Y_2O_3–ZrO_2 systems [9–11], and in relation to the viscosity of the grain boundary phase [12–15]. Both the product and the rate of oxidation have been shown to be strictly related to chemical composition [13, 14, 16]. The present study focuses on the oxidation phenomenology in Si_3N_4–Al_2O_3–ZrO_2 and Si_3N_4–Al_2O_3 materials.

2. Experimental

2.1. Materials

Samples of the following compositions were uniaxially hot pressed at 34.4 MPa in 10^{-3} vacuum atmosphere:

AZ: 83 wt % Si_3N_4–5 wt % Al_2O_3–12 wt % ZrO_2

A: 95 wt % Si_3N_4–5 wt % Al_2O_3

Hot-pressing conditions, crystal phases and some parameters of the microstructure of the hot-pressed materials are summarized in Table I. Details of preparation techniques, microstructure and mechanical properties have been reported elsewhere [17].

The development of microstructure occurs through liquid phase sintering, possibly accompanied by some evaporation–condensation phenomena which leads to a limiting density [17].

The specific mechanism suggested for the $\alpha \rightarrow \beta'$-SiAlON conversion features a continuous change of the Al content in the grain boundary phase [17], which is related to the degree of the $\alpha \rightarrow \beta'$ conversion which has been evaluated through the $\beta'/(\alpha + \beta')$ ratio. Oxidation studies have been performed on selected samples: AZ1, AZ3, AZ4 for the Si_3N_4–Al_2O_3–ZrO_2 composition, and A1, A2 for the Si_3N_4–Al_2O_3 composition, i.e. on materials exhibiting very different $\alpha \rightarrow \beta'$ conversion degrees.

2.2. Oxidation tests

Short term (30 h) oxidation tests were carried out at 873 K $\leqslant T \leqslant$ 1763 K in 98 KPa air atmosphere on 10 × 10 × 2 mm^3 polished and ultrasonically cleaned samples, diamond sawn from the hot-pressed billets.

Weight gain was continuously recorded using a

TABLE I Hot pressing parameters and some features of the microstructure for the AZ and A samples [17]

Sample	Hot pressing parameters		Bulk density %	Residual α-Si_3N_4	$\beta'/(\alpha+\beta')$	X-ray semiquantitative evaluation of crystalline phases					
	T (K)	t (min)				m-Z_2O_2	$t-Z_2O_2$	Si_2N_2O	X-SiAlON	Si_3N_4	Si_3N_4
AZ1	1813	30	93	–	87.0	0.13	22	7	3	3	56	9
AZ2	1853	30	95	0.48	68.0	0.32	22	7	7	3	41	20
AZ3	1923	60	97	0.72	28.0	0.72	13	8	8	3	20	48
AZ4	1923	120	97	0.85	26.0	0.74	13	8	8	3	17	51
AZ5	1923	220	97	0.90	8.0	0.92	15	5	8	3	6	63
AZ6	1973	120	98	1.00	6.5	0.94	16	3	5	2	5	69
A1	1923	60	95	0.56	69.0	0.31			9	traces	63	28
A2	1923	120	98	0.85	40.0	0.60			10	2	34	54
A3	1923	220	99	0.93	13.5	0.87			7	2	9	82

0022–2461/88 $03.00 + .12

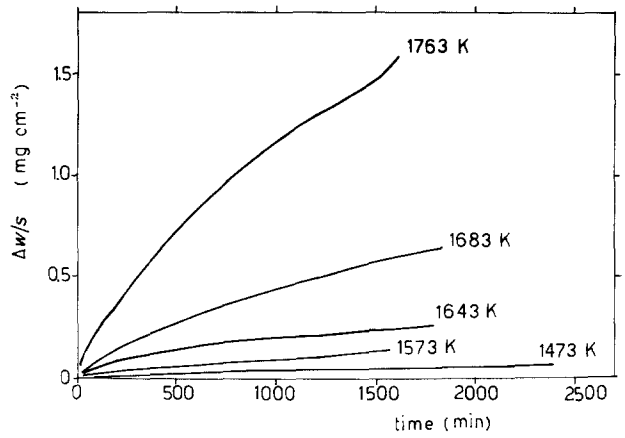

Figure 1 Weight gain for sample AZ1 oxidized at various temperatures at 98 kPa in air.

TG apparatus* capable of 2×10^{-5} g resolution. The heating and cooling rates were 20 – 10 k min^{-1}. Long term (100 and 400 h) oxidation tests were also performed in an electric laboratory kiln; before and after oxidation, the samples were weighed to ± 10 g accuracy.

Surface and cross-sections of the oxide scales were analysed by X-ray diffraction analysis (XRD)†, SEM‡ including back-scattering electron imaging (BSE), WDS§ and EDS¶. The crystalline phase content of the oxide-layer surface was evaluated from room temperature semiquantitative XRD.

3. Results and discussion

3.1. Oxidation kinetics

Short term oxidation has been extensively studied for the sample AZ1 at 1473 K to 1763 K. Weight gain follows the classical parabolic relation (Fig. 1)

$$W^2 = Kt + b \simeq Kt$$

where $W = \Delta w/S$ is the weight gain (mg cm^{-2}) at time', $K = K_0 \exp(\Delta H/RT)$ (mg^2 cm^{-4} min^{-1}) is the

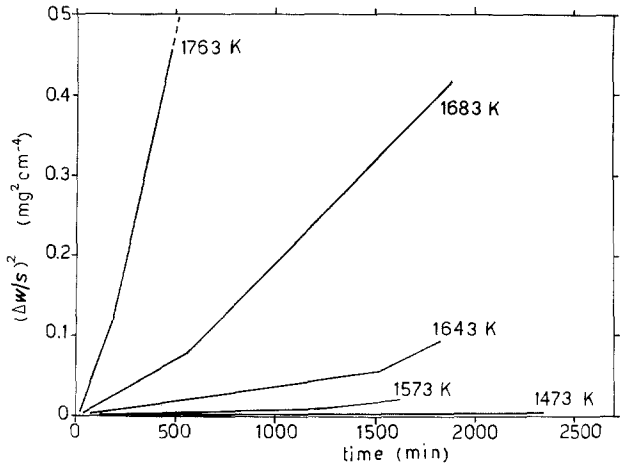

Figure 2 Parabolic weight gain for sample AZ1 oxidized at 98 kPa in air.

*Netzsch Geratebau, W. G.
†SIEMENS D.500, Cu Kα, Ni filter
‡Autoscan, Etec. Corp., USA
§Autospec, Etec. Corp., USA
¶EDAX PV 9100, Philips

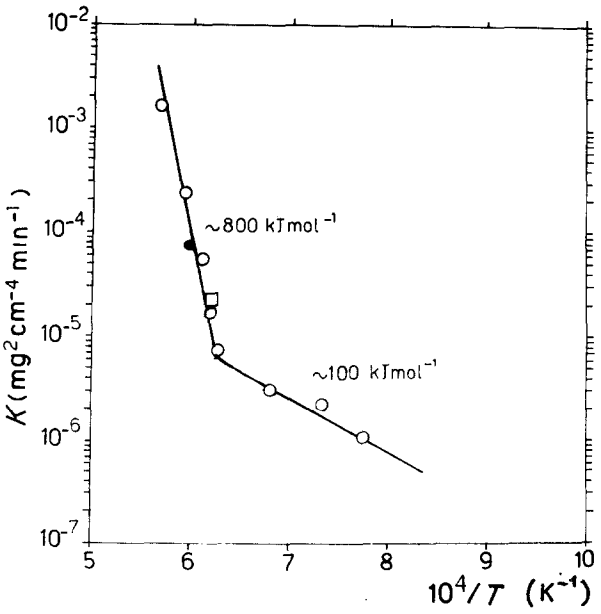

Figure 3 Arrhenius plot of oxidation rate constants derived from Fig. 2. ○ sample AZ1 (30 h), ● sample AZ3 (30 h), □ sample AZ4 (100 h).

parabolic rate constant and b is a constant which accounts for the effect of a possible non-parabolic initial stage, i.e. for the uncertainty of the exact definition of the beginning ($t = 0$) of the parabolic process. The existence of two different parabolic oxidation regimes is shown by the $(\Delta w/S)^2$ plots of Fig. 2, the breakpoint shifting to longer times with decreasing oxidation temperature.

The Arrhenius plot (Fig. 3) of the rate constant K (evaluated on the overall range of oxidation times) results in two well defined oxidation regimes.

The low temperature regime (up to ~1600 K) is characterized by an apparent activation energy (ΔH) of ~100 kJ mol^{-1}, whereas a much higher ΔH value of ~800 kJ mol^{-1} corresponds to the high temperature regime (~1573–1773 K). Additional short term oxidation tests were carried out on sample AZ3 (Fig. 3) and on samples Al and A3. Long term tests (100 h and 400 h) were performed on samples AZ4 and A2 at 1573 K. Oxidation rate constants, evaluated on the assumption of parabolic behaviour throughout the overall duration of the long term tests (Table II), offer data consistent with the short term tests only for the 100 h run. Substantially lower oxidation constants are evaluated for the 400 h test, this possibly accounts for some modification in the oxidation phenomenology.

TABLE II Values of the oxidation rate constant after different durations of the oxidation tests at $T = 1573$ K

Material	Oxidation rate constants (mg^2 cm^{-4} min^{-1})		
	30 h	100 h	400 h
AZ4	1.6×10^{-5}	1.7×10^{-5}	6.0×10^{-6}
A2	1.0×10^{-5}	1.4×10^{-5}	8.0×10^{-6}

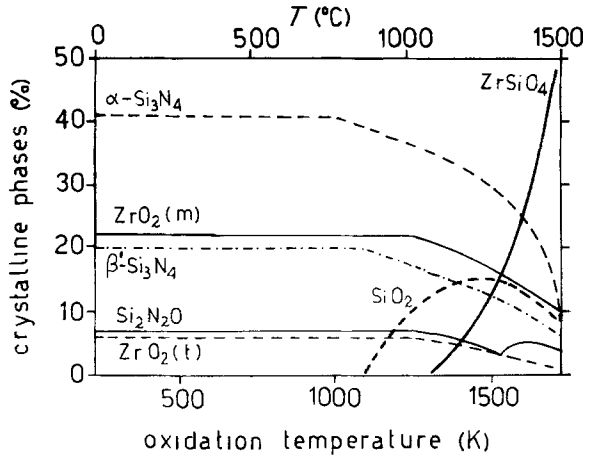

Figure 4 XRD evolution of crystal phases in sample AZ2 after 30 h oxidation in air.

No detectable oxidation occurs at $T < 1273$ K; this supports the theory that no easy-to-oxidize zirconium oxynitride phases are present [16].

3.2. Structure and morphology of the oxide scale

Fig. 4 shows typical semi-quantitative XRD results for the crystal phase contents of the surface of the oxide scale for AZ samples. The most apparent feature is the abrupt crystallization of zircon at $T > \sim 1473$ K and the related decrease in crystobalite. The evolution of the surface morphology of the oxide, shown in Fig. 5 a–f, includes, as main features, formation of a thin glassy layer at an early temperature regime (Fig. 5a) followed by a number of complex modifications like the formation of crystal phases and their dissolution up to the extreme features, depicted in

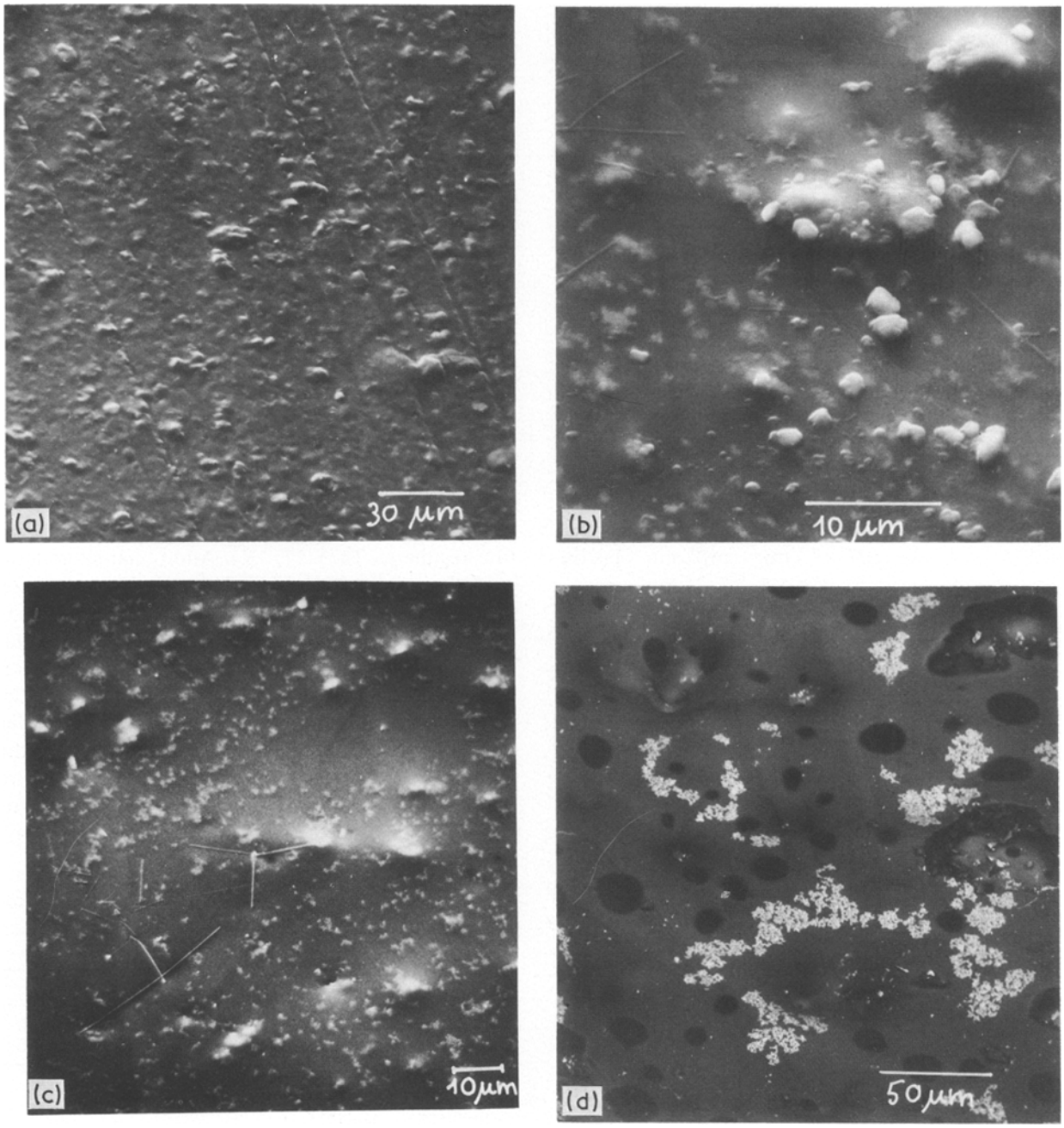

Figure 5 Scanning electron micrographs of the oxidized surface of AZ2 sample after 30 h oxidation in air: (a) $T = 1363$ K, (b) $T = 1473$ K, (c) $T = 1573$ K, (d) $T = 1683$ K, back scattered electron image; (e) $T = 1763$ K, back scattered electron image; (f) glass spherulites developed at 1763 K inside large holes deriving from bubble bursting.

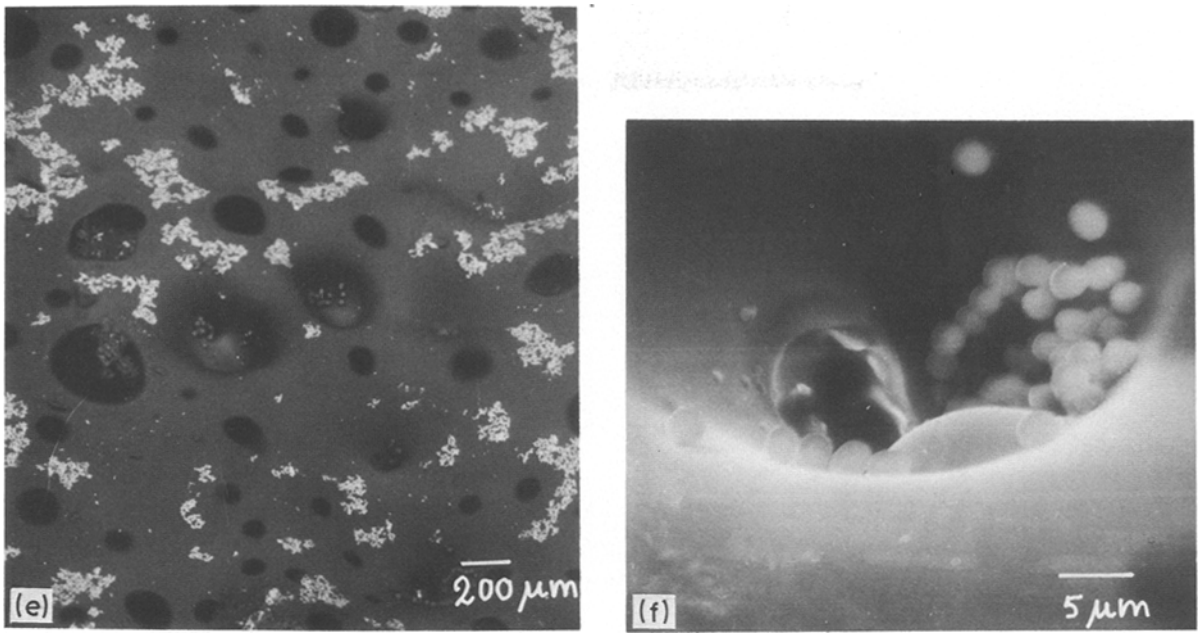

Figure 5 Continued

Fig. 5d–e, where large bubbles, escape pores and a population of $ZrSiO_4$ crystals make up the morphological aspect. Small glass spherulites appear inside large pores as probable relics of the bursting of bubbles (Fig. 5f).

Fig. 6 is a backscattered electron image of the cross-section of the oxide scale. The glassy oxide contains relevant amounts of aluminium, potassium, calcium and magnesium but not of zirconium, which is detected only combined in $ZrSiO_4$ crystals.

Long term oxidation tests in AZ samples result in morphologies similar to short term tests at a corresponding temperature (Fig. 7a, b) and show a well developed population of $ZrSiO_4$ crystals. Crystobalite is the only crystal phase detected by XRD in Si_3N_4–Al_2O_3 samples. The evolution of morphology includes formation of a thin glassy oxide film at $T > \sim 1473$ K and formation at higher temperatures of limited, X-ray undetectable, amounts of Al-rich elongated crystal forms (Fig. 8a), probably mullite as suggested by elemental WDS analysis, which grow in the proximity of pore clusters in the hot-pressed sample. A heavily cracked and spalled, thin potassium, calcium, magnesium rich oxide layer containing a network of needle-like crystobalite (Fig. 8b) is the main feature at the higher oxidation temperatures. The surface of the A3 sample subjected to long term oxidation tests at 1573 K looks bright, covered by a glassy cracked layer rich in aluminium and metal impurities, and containing hollows, escape pores and irregular shapes (Fig. 9).

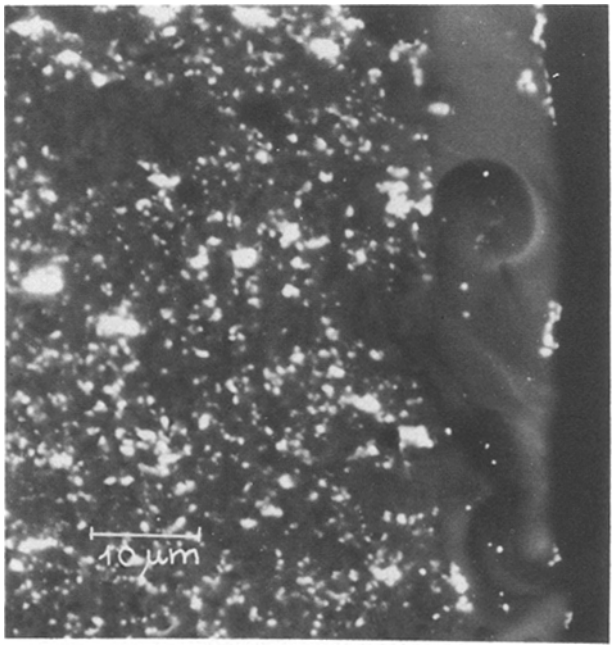

Figure 6 Cross-section image of the sample oxidized at 1573 K, back scattered electron image.

3.3. Discussion of the oxidation mechanism

The oxidation resistance of Si_3N_4–Al_2O_3–ZrO_2 composites at relatively low temperatures proves to be much better than that for binary Si_3N_4–ZrO_2 composites [9–11]. This derives from the absence of Zr–O–N phases which undergo the catastrophic oxidation that has been shown to dramatically affect oxidation performance of Si_3N_4–ZrO_2 materials [9–11] at $\sim 873 < T < \sim 1273$ K. ZrO_2 it is not like to directly affect oxidation, the substantial amounts of $ZrSiO_2$ formed in the oxide scale at $T > \sim 1600$ K possibly being a result of a chemical reaction of ZrO_2 with SiO_2 at the oxide–nitride interface. Nevertheless some indirect effects cannot be excluded *a priori* because of solubilization–reprecipitation of zirconium-based compounds which affects the viscosity of the oxide film. Furthermore, the oxidation behaviour of both the Si_3N_4–Al_2O_3–ZrO_2 and the Si_3N_4–Al_2O_3 materials is substantially better than for other Si_3N_4-based systems [5, 9–14, 18, 19] on the whole range of temperatures investigated. Fig. 10 compares the oxidation weight gains at 1573 K and Fig. 11 the oxidation rate constants for different HPSN systems. It is well known that the oxidation resistance of β'-SiAlON is higher

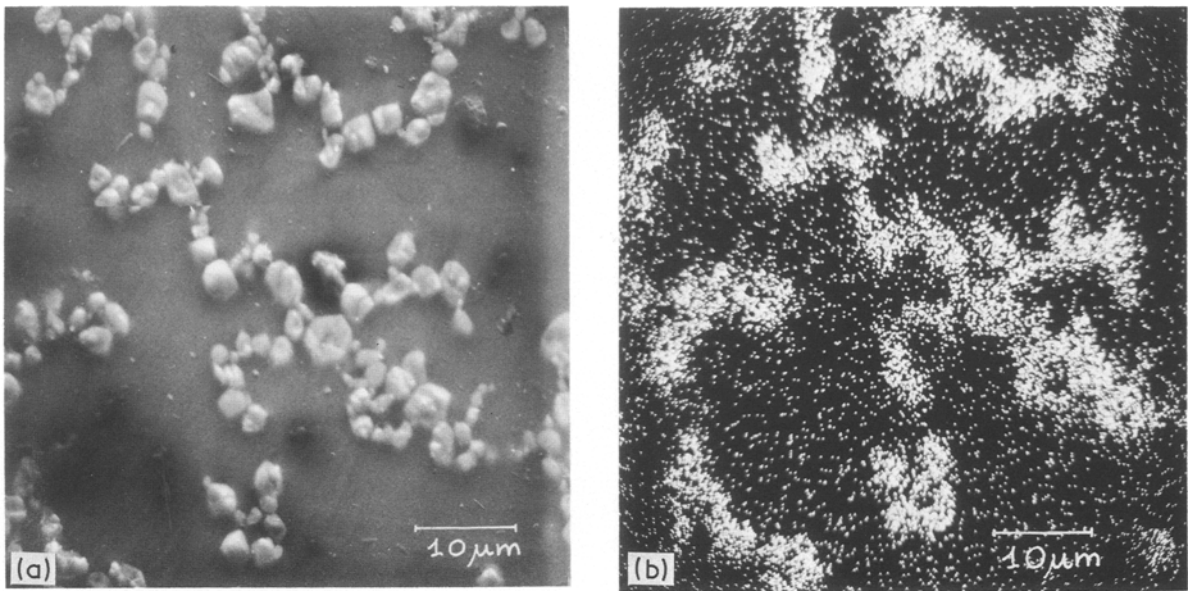

Figure 7 Oxidized surface of the sample AZ2 after 400 h oxidation at 1573 K; (a) morphology, (b) X-ray map of Zr.

than that for α- and β-Si_3N_4. This also reflects in the oxidation behaviour of polycrystalline ceramics [20].

The experimental evidence gained suggests that: (i) no detectable difference in oxidation rate exists among materials substantially differing in the amount of β′-phase, and (ii) no continuous crystalline mullite layer is observed; needle-like mullite, when present, occurs as a very minor constituent within the oxide. Therefore, the conclusion can be drawn that the oxidation behaviour in our materials is neither controlled by the actual amount of B′-SiAlON, nor by protective mullite layers [15, 20–22].

WDS elemental analyses and theoretical calculations of the β′-s.s. for differently converted samples suggest that a substantial amount of the Al_2O_3 is combined in the β′ lattice, irrespective on the amount of α converted. Thus the overall aluminium amount in the residual grain boundary phase should be limited. If the fact that in SiAlON ceramics with residual glass, the concentration of aluminium in the glass is normally much higher than in β′ is taken into consideration it might suggest that the amount of grain boundary phase in our materials is relatively scarce. Both the viscosity of the residual grain boundary phase and oxide film have been recognized as key factors for oxidation [13–15, 23] and offer a chance to discuss the present data.

At low oxidation temperatures (i.e. $< \sim 1600$ K), mobility in the high viscous grain boundary phase is low and oxidation possibly occurs by the classical reaction of oxygen with Si_3N_4. The low apparent activation energy (~ 100 kJ mol^{-1}) for the process within this temperature range (Fig. 3) is typical for oxygen diffusion in silicates, so that the governing step of the oxidative process might be at this stage oxygen diffusion through the silica oxide layer towards the reactive interface. A similar oxidation mechanism has been suggested for SiAlON materials [20].

The breakpoint in Fig. 3 corresponds to a substantial decrease of the viscosity of the grain boundary

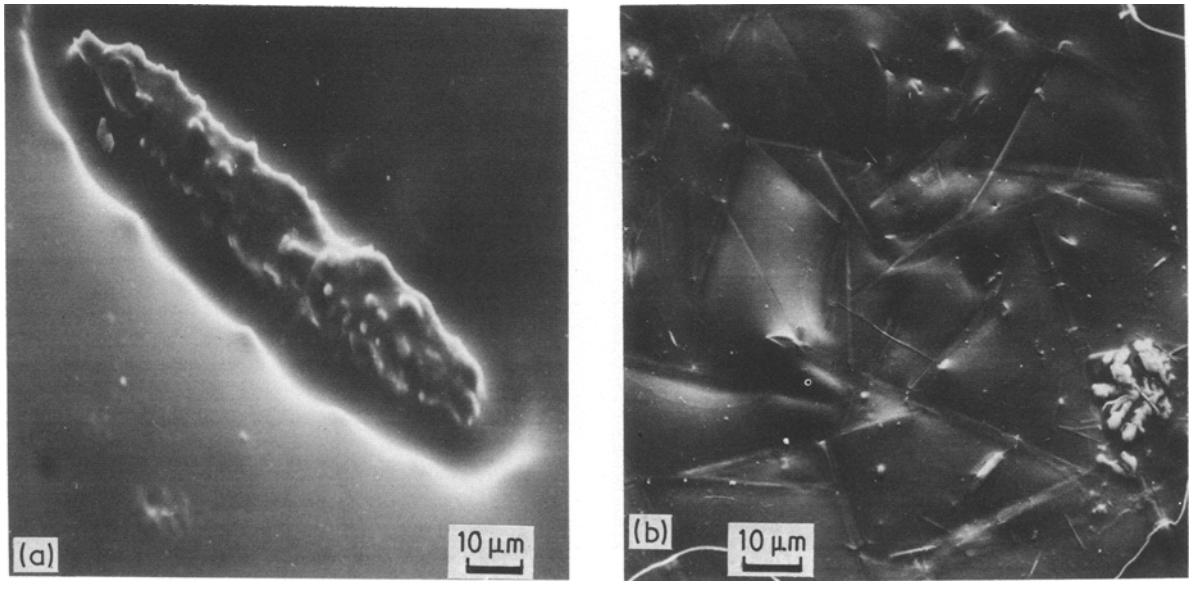

Figure 8 (a) oxidized surface of sample A1 after 30 h oxidation at 1473 K; (b) oxidized surface of the sample A2 after 30 h oxidation at 1473 K.

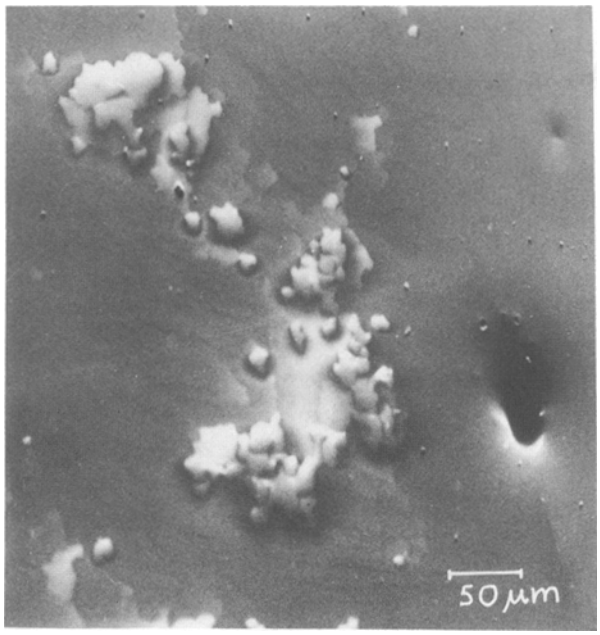

Figure 9 Surface of A3 sample after 400 h oxidation at 1573 K.

phase which occurs at ~1600 K and allows metal cation impurities (potassium, calcium, sodium, magnesium) to migrate more easily to the oxide scale. A complex reaction pattern thus occurs at the reaction interface among nitride phases, silica and impurities which is either governed by chemical reaction or by diffusion according to the actual rates of the corresponding processes. Oxygen diffusion seems no longer to be the limiting step for oxidation. Cation diffusion within the grain boundary phase would probably become limiting, as reflected by the value of the apparent activation energy for oxidation (~800 kJ mol^{-1}), which recalls the diffusion of metal cations in a viscous silicate melt. This leads to a progressive depletion of metal impurities in the grain boundary phase and to a corresponding increase of its viscosity.

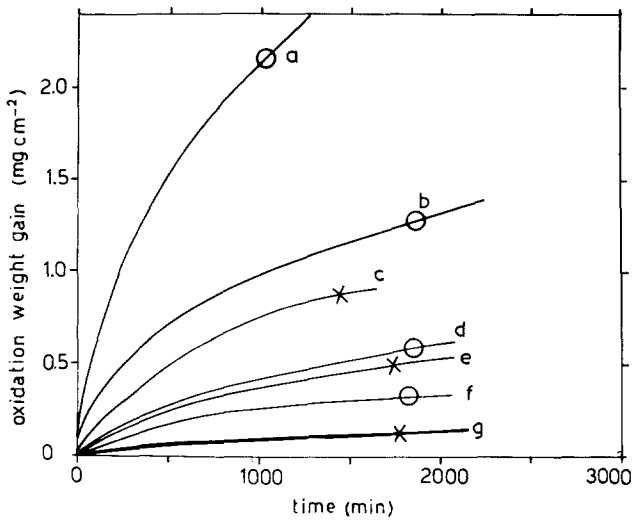

Figure 10 Oxidation weight gain at 1573 K for different hot pressed silicon nitride-based materials, showing the excellent behaviour of the Si_3N_4–Al_2O_3–ZrO_2 system. o impure Si_3N_4 powder (AME R.G), x pure Si_3N_4 powder (Starch LC 10). (a) 5 wt % MgO, (b) 1 wt % MgO + 8 wt % Y_2O_3, (c) 3 wt % MgO + 12 wt % ZrO_2, (d) 10 wt % CeO_2, (e) 3 wt % MgO, (f) 6 wt % SiO_2 + 12 wt % Y_2O_3, (g) 5 wt % Al_2O_3 + 12 wt % ZrO_2.

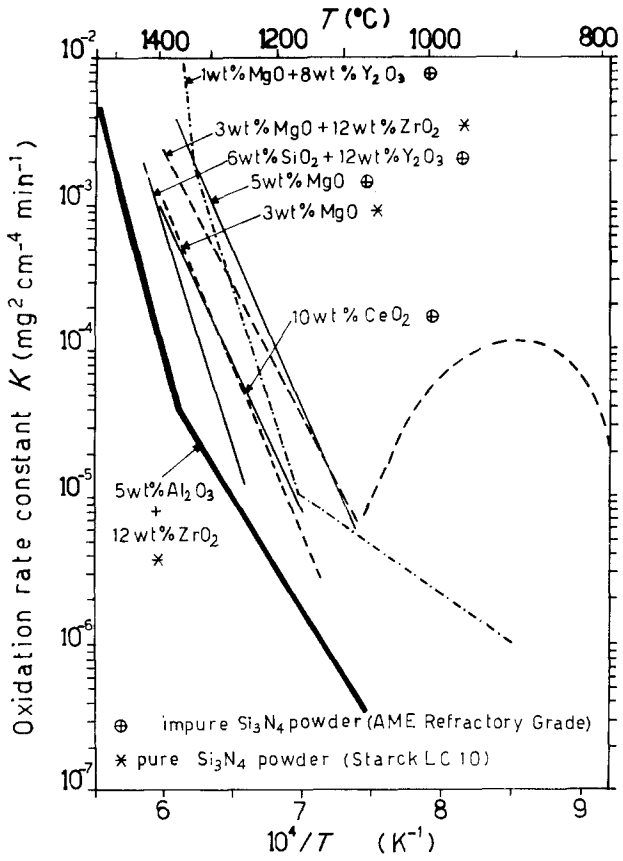

Figure 11 Arrhenius plot of the oxidation rate constants for silicon nitride hot pressed in various systems, showing the highest oxidation resistance of the Si_3N_4–Al_2O_3–ZrO_2 materials.

Viscosity of the oxide scales also may be an important feature for both the oxide microstructure and the oxidation kinetics. Its effect on nitrogen bubbles nucleation, growth and transport within the oxide scales has well been recognized [23]. Low viscosity allows both outward atomic nitrogen diffusion and inward oxygen diffusion to occur easily; at increased viscosity, nucleation and growth of nitrogen bubbles is more likely to occur, because of the reduced solubility of nitrogen in the oxide. Bubble cross-flow occurs throughout the film towards the surface, where they are burnt, resulting in the uneven surface topography in cooled specimens, shown by SEM micrographs.

The change of oxidation kinetics with time shown by the $(\Delta w/s)^2$ against time plots of Fig. 2, can possibly be related to the increased generation and release rate of nitrogen bubbles in a highly viscous liquid which results in an open channel path for incoming oxygen, i.e. the oxide film locally loses its protective character. Nevertheless, no linear components of the oxidation kinetics have been appreciated at prolonged exposure times to clearly support a non-protective contribution to oxidation, although the shift towards shorter times of the beginning of the second faster parabolic stage of oxidation with increasing oxidation temperature, a feature which also has been previously pointed out [22, 24], might represent a time-dependent viscosity effect. Despite the strong dependence on temperature at T ~1600 K of the oxidation rate constants (Fig. 3), the overall oxidation behaviour of both Si_3N_4–Al_2O_3–ZrO_2 and Si_3N_4–Al_2O_3 materials is

outperforming a number of other HPSN systems (Fig. 11). This might possibly derive from the total flux of reacting species being limited by

(i) the scarce amount of grain boundary phase in both the AZ and A materials, their overall Si_3N_4 and Al_2O_3 contents approaching the theoretical β'-Si_3N_4 line, and

(ii) the less solubility of Si and N in the Al_2O_3-rich, viscous oxide film, and possibly

(iii) the decreased solubilization rate of the nitride phases in the highly viscous oxide film.

4. Conclusions

The extremely good performance of Si_3N_4–Al_2O_3–ZrO_2 composites in oxidizing environments is related to

(i) absence of Zr–O–N phases which have been found to dramatically affect oxidation in other additive sintered or hot-pressed silicon nitride materials containing ZrO_2;

(ii) low amount of grain boundary phase, and

(iii) decreased dissolution rate at the nitride/high viscous oxide film interface.

The presence of Al_2O_3 inhibits formation of Zr–O–N phases, irrespective of its distribution within the nitride phases. Two oxidation regimes with very different apparent activation energies reflect the possible governing mechanisms of the process, i.e. oxygen diffusion through the oxide film at a low temperature regime ($T < \sim 1600\,K$) and metal cation diffusion at higher temperatures.

References

1. A. J. KIEHLE, L. K. HEUNG, P. J. JELISSE and T. J. ROCKETT, *J. Amer. Ceram. Soc.* **58** (1975) 17.
2. S. C. SINGHAL, *J. Mater. Sci.* **11** (1976) 500.
3. D. CUBICIOTTI and K. H. LAU, *J. Electrochem. Soc.: Solid State Sci. Technol.* **126** (1979) 1724.
4. G. N. BABINI, A. BELLOSI and P. VINCENZINI, *Ceram Int.* **7** (1981) 78.
5. *Idem. J. Amer. Ceram. Soc.* **64** (1981) 578.
6. S. C. SINGHAL, in "NATO/ASI Nitrogen Ceramics", edited by F. L. Riley (Noordhoff, London, 1976) p. 607.
7. F. F. LANGE, S. C. SINGHAL and R. C. KUZNICKI, *J. Amer. Ceram. Soc.* **60** (1977) 249.
8. R. R. WILLS, J. A. CUNNINGHAM, J. M. WIMMER and R. W. STEWART, *ibid.* **59** (1976) 269.
9. G. N. BABINI, A. BELLOSI, P. VINCENZINI, D. DALLE FABBRICHE and R. VISANI, in "Science of Ceramics" Vol. 12, edited by P. Vincenzini (Ceramurgica S.r.l., Faenza, 1984) p. 471.
10. G. N. BABINI, A. BELLOSI and P. VINCENZINI, in "Reactivity of Solids" Vol. 10, edited by P. Barret and L. C. Dufour (Elsevier, Amsterdam, 1985) p. 827.
11. P. VINCENZINI, A. BELLOSI and G. N. BABINI, *Ceramics Int.* **12** (1986) 133.
12. G. N. BABINI, A. BELLOSI and P. VINCENZINI, in "Science of Ceramics" Vol. 11, edited by R. Carlsson and S. Karlsson (Swedish Ceramic Society, Gothenburg, 1981) p. 291.
13. G. N. BABINI, A. BELLOSI and P. VINCENZINI, *J. Mater. Sci.* **19** (1984) 1029.
14. *Idem. ibid.* **19** (1984) 3487.
15. M. H. LEWIS and P. BARNARD, *ibid.* **15** (1980) 443.
16. D. R. CLARKE and F. F. LANGE, *J. Amer. Ceram. Soc.* **63** (1980) 586.
17. A. BELLOSI, P. VINCENZINI and G. N. BABINI, *Mater. Chem. Phys.* **18** (1988) 205.
18. G. N. BABINI, A. BELLOSI and P. VINCENZINI, *La Ceramica* **3** (1981) 11.
19. *Idem., J. Mater. Sci.* **17** (1982) 23.
20. J. SCHLICHTING, "NATO/ASI Nitrogen Ceramics", edited by F. L. Riley, (Noordhoff, London, 1977) p. 627.
21. K. H. JACK, *J. Mater. Sci.* **11** (1976) 1135.
22. Y. T. HASEGAWA, K. HIROTA, T. YAMANE, M. MITOMO and H. SUZUKI, *Yogyo-Kyokai-Sci.* **89** (1981) 148.
23. J. DESMAISON, M. BROSSARD, M. DESMAISON-BRUT and P. GOURSAT, in "Nitrogen Ceramics", edited by F. L. Rieley, (Martinus Nijhoff, The Hague, 1983) p. 439.
24. S. DUTTA, *J. Amer. Ceram. Soc.* **59** (1980) 623.

Received 10 February
and accepted 22 October 1987